A search for active star-forming galaxies with the ESO 1 meter Schmidt telescope

C. Surace, G. Comte

Astron. Astrophys. 281, 653–665 (1994)

ASTRONOMY AND ASTROPHYSICS

A search for active star-forming galaxies with the ESO 1 meter Schmidt telescope*

C. Surace and G. Comte

Observatoire de Marseille, 2 Place Le Verrier, F-13248 Marseille, France

Received April 29, accepted August 6, 1993

Abstract. A new search for active galaxies has been conducted using the ESO 1 meter Schmidt telescope, in order to build a sample of emission lines and ultraviolet excess objects. The observational strategy was focussed on getting deeper detection and better completeness on faint apparent magnitude objects than those obtained in preceding surveys. The reduction procedure aims at a maximum astrophysical output before any complementary follow-up, thus we expect an easy selection of interesting targets from the catalog of candidate galaxies (to be published later) when future observations will be planned. The redshifts are measured on Schmidt objective prism plates with a mean accuracy of 160 km s^{-1}. This accuracy has been checked by means of published velocities up to 5000 km s^{-1}, but the emission line galaxies detected have redshifts up to $z=0.06$. The R magnitudes, (U-R) colors, isophotal diameters, surface brightnesses and quantitative morphological parameters are derived from U/R bicolor direct plates. Colors are tied to the U, R Basel system by means of a statistical comparison of the field star instrumental color distribution with the field star Basel color distribution at a symmetric Galactic latitude. The accuracy of the $(U-R)_{Basel}$ zero point is at best 0.10 magnitude. The asymptotic R magnitudes are calibrated in Cousins system with ESO-LV small diameter galaxies, and are thought to be accurate to 0.30 magnitude. The expected limiting R magnitude of the survey is 18.5 The present paper is limited to a description of the methodology, illustrated with preliminary results obtained in two fields.

Key words: surveys – galaxies: general galaxies: distances and redshifts – galaxies: starburst – techniques: images processing

1. Introduction

Starburst galaxies include a large variety of objects, from normal spirals with circumnuclear bright hot spots or active ringed structures to ultraluminous IRAS infrared sources recently recognized as merging systems. Numerous other types are found, specially the so called HII galaxies (Terlevich et al. 1991). In current theories of galaxy formation, (see e.g. White, 1988 for a review), normal galaxies experienced an initial violent burst of star formation before evolving towards the different kinds we observe at zero redshift. Hence, if galaxy formation were still taking place to-day, one expects some starburst systems to be primeval galaxies.

Starburst galaxies can be easily recognized thanks to the massive stars produced during the burst. These stars enhance the blue and near ultraviolet continuum of the object. The O stars radiate hard ultraviolet flux able to ionize the interstellar gas which shows bright emission lines. Some IRAS sources are starburst galaxies: if the objects are dust-rich, ultraviolet flux is partly absorbed by the dust which reradiates in the far infrared (60-100 μm).

Some important astrophysical problems are still unanswered in spite of continuous progress in the observation and interpretation of starburst phenomena. For example, the following questions are still pending: correct determination of the luminosity function of active star-forming galaxies with respect to "normal" field galaxies, (see Salzer 1989 and Comte et al. 1993 for a discussion); the abundance-luminosity relationship, still controversial; the search for extreme metal-deficient star-forming galaxies; the identification of triggering mechanisms for the starbursts; the frequency of occurrence of starbursts and possible links with the environnement; the determination of the age spectrum of the bursts among the galaxian population.

To address these problems, statistical studies over large samples of objects are required. These samples must contain galaxies of various luminosities in sufficient number, (specially low-luminosity ones), of various morphological types, of various metallicities and with the starburst seen at different evolutionary stages: from the zero-age burst (no sign of evolution either in the stellar population or in the emission spectrum) to the ending phases of an old burst (dying emission spectrum of low excitation, or blueish color without emission). The presence of low-luminosity objects in significant numbers implies that the samples have to be produced by a deep survey. However,

* Based on plates obtained with the European Southern Observatory 1 meter Schmidt telescope at La Silla (Chile) and digitizations made with the MAMA measuring machine of C.A.I. (INSU Paris)

Send offprint requests to: C. Surace

if one observes small sky areas at very deep limiting magnitudes, the galaxian population seen is dominated by relatively high-redshift objects and results may be complicated by cosmological evolution effects. Therefore, a deep but quite large field survey is necessary to select a small redshift population. To observe various evolutionary stages of the starbursts implies that the survey associates field spectroscopy to find emission line objects and color search to find blue color objects. Such a twofold selection, color and emission line, has already been combined in the Second Byurakan Survey (Markarian & Stepanian 1983) and in the Case Survey (Pesch & Sanduleak 1983 and later), for instance.

Up to now, most catalogs produced from photographic Schmidt telescope searches for active extragalactic objects contain a quite small amount of information. Positions, apparent magnitudes generally affected by unknown but possibly substantial errors, colors which generally are not on any standard scale (for color surveys), eye estimates of emission line strengths and very crude estimates of redshift (for emission lines surveys). The astrophysical exploitation therefore needs long term timeconsuming follow-up programs on 2 meter-class telescopes (Bothun et al. 1989; Salzer et al. 1989; Augarde et al. 1993).

The present paper describes a photographic survey for active star-forming galaxies conducted with the European Southern Observatory 1 meter Schmidt telescope. We used the telescope in two different modes: search for emission line galaxies with the objective prism and search for ultraviolet excess galaxies by means of double exposures on direct plates in U and R. We present below the methodology and the reduction procedure which has been developed to maximize the astrophysical content of the candidate objects catalog. A very preliminary discussion of some results obtained on two fields located in the direction of the southern extension of the Virgo Supercluster illustrates the potential interest of the survey. The complete catalog of data on these two fields will appear elsewhere, as well as a more elaborate astrophysical analysis.

2. Observations

We used the ESO 1 meter Schmidt telescope to take 4 exposures for each field:

- 2 prism plates, on IIIaJ emulsion through the large dispersion 4° objective prism. The plates are doubled in order to remove uncertain detections, confirming some objects after checking on the twin plate. The spectral sensitivity of the emulsion constrains the spectrum range to about 1900 Å, from 3400 Å to 5300 Å. This allows us the detection of the emission lines [OIII], H_β, [OII], sometimes H_γ and [NeIII]. Because of the IIIaJ sensitivity cutoff, the [OIII] lines can be seen till $Z = 0.06$.

A sky-limited exposure of 100 minutes limits the continuum magnitude to an estimated value of 17 to 17.5 but sometimes fainter objects with large equivalent width emission lines can be detected.

- 1 bicolor plate: 2 exposures with 2 different filters on the same plate. The second exposure is offseted by 30 arc seconds along the declination axis from the first one. We used IIIaF plates which combine a fine grain, high detective quantum efficiency and good spectral sensitivity both in the uv-blue and the red. Exposure times are balanced with respect to the relative sensitivity of the emulsion in both passbands as follows: the plate is exposed 25 minutes through a RG630 filter and 80 minutes through an UG11 filter. Any object bluer than an approximate equivalent F5 spectral type appears with an U image brighter than the R one. From the transmission curve of the Schott filters UG11 and RG630 (given in Schott technical notices), the average spectral sensitivity curve of Kodak IIIaF emulsion (and in the ultraviolet, the transmission curve of Schott UK50 material of the Schmidt corrector) we have computed the definition of our instrumental passbands as follows:

U_{inst} has an effective wavelength λ_{eff} of 3640 Å and a width at half maximum $\Delta\lambda$ of 665 Å, out of the atmosphere, for a flat spectrum. λ_{eff} may be slightly shifted towards longer wavelengths, and $\Delta\lambda$ reduced, due to atmospheric absorption at short wavelength, but this effect is difficult to evaluate.

R_{inst} has an effective wavelength of 6610 Å and a width at half maximum $\Delta\lambda$ of 660 Å.

These values may be compared with the U and R bands of Basel photographic photometry (U_{Basel}: $\lambda_{eff} = 3660$ Å, $\Delta\lambda = 565$ Å ; R_{Basel}: $\lambda_{eff} = 6380$ Å, $\Delta\lambda = 510$ Å). Our instrumental system filters the stellar spectra with a very similar ultraviolet band as does the Basel system (the long wavelength half of both passbands are practically identical which is important because of the presence of strong line blanketing and Balmer jump in this range). Our R band is redder than the Basel one but this normally should appear bothersome only for the coldest stars rich in TiO_2 and ZrO_2 molecular features.

For point sources, the limiting magnitude of these direct images is around 19.5 in the red. Two fields located on Virgo south extension and nearby areas were observed from March to May 1989 at the European Southern Observatory (ESO) at La Silla (Chile).

Fields are centered at:

$13^h12^{mn}00^s$	$-20°30'00''$	
$13^h12^{mn}53^s$	$-25°10'05''$	(1950.0)

3. Digitization of the plates and calibrations

3.1. Target selection

Total digitization of large Schmidt plates produces a considerable amount of data whose processing, unless fully automated, is very difficult. A 30 cm square plate scanned with a step size of 10 μm and a slit of 10 μm generates 900,000,000 pixels, more than 95% of which are blank sky and contain almost no information. Therefore we decided to use the classical method of preselection of candidate objects by eye examination, using binocular microscope. To ensure a more reliable visual search, two different persons inspect the plates. A final list is established after a careful cross verification of the detected objects. Positions of the selected objects have been measured using the X-Y

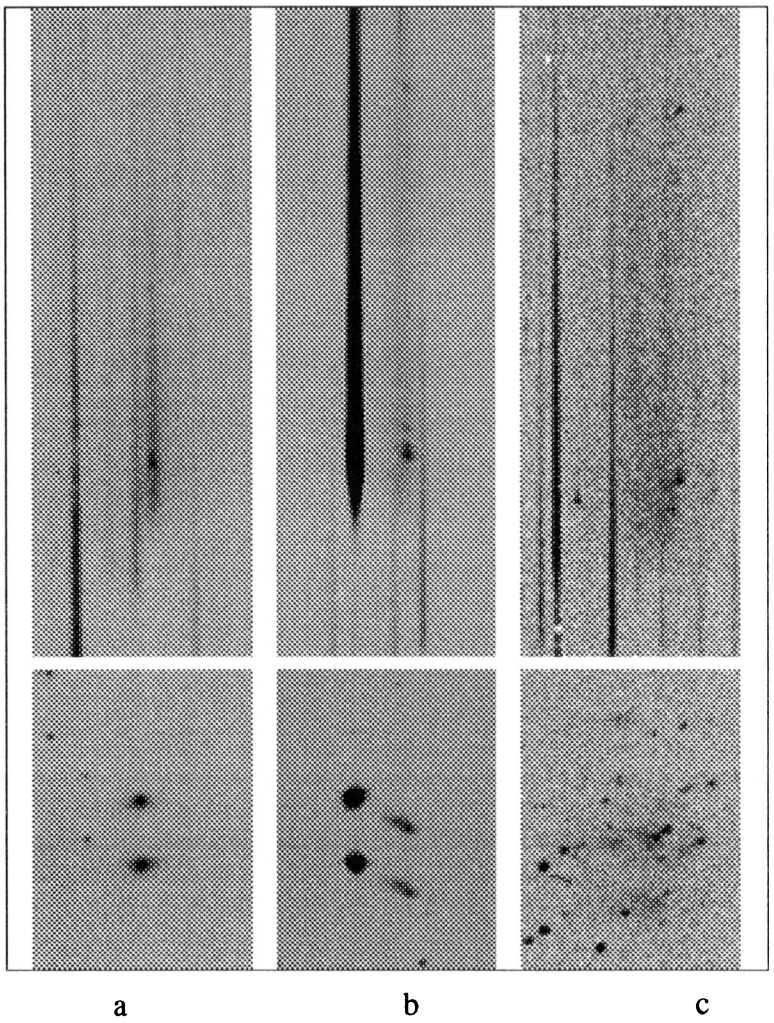

Fig. 1a–c. Emission line galaxies and their spectra. *bottom*: images from bicolor plates (U exposure: upper image; R exposure: lower one) *top*: spectra extracted from objective prism plate (green end is at the bottom of the frame) **a** low excitation nuclear HII region **b** high excitation region in distorted system **c** HII regions in the arms of a low surface brightness spiral

machine at Observatoire de Marseille. The astrometric reduction of these positions have been done using the Perth70 catalog of astrometric standards (Høg et al. 1976) and the program XY-POS written by R.M. West.

Figures 1 and 2 show examples of objects selected by the visual search on the plates.

3.2. Digitization

The MAMA machine (Machine A Mesurer pour l'Astronomie) of Observatoire de Paris was used for plate digitization. The MAMA machine is a fast microdensitometer specifically built to scan large format plates, with a self-scanned Reticon diode array as detector (Guibert et al. 1984; Berger et al. 1991; Guibert & Moreau 1991; Soubiran 1992). It offers very good positional accuracy and reproducibility (a fraction of micron for a 30 cm field). The normal output of the MAMA machine are block scans with a pixel size of 10x10 μm^2 with a step size of 10 μm. An array processor which performs several real time pre-processing tasks may also be used to rebin the original pixels in larger ones ensuring flux conservation.

Small block scans were recorded on the plates. The parameters of these scans after rebinning in the array processor are:

- on prism plates, block scan of $512 \cdot 512 \cdot 20$ μm^2 dimension centered on each candidate emission line spectrum.
- on bicolor plates, block scans of either $512 \cdot 512 \cdot 20$ μm^2 dimension or $1024 \cdot 1024 \cdot 20$ μm^2 dimension depending on the local projected density of ultraviolet excess candidates.

The step size was 20 μm in all cases.

3.3. Density-intensity calibration

The MAMA machine produces photographic density files which must be converted into intensity files. Smaller plates cut from the same box of emulsion were exposed in the ESO spot sensitometer providing arrays of 21 spots. These were also scanned with the MAMA, using large (80 μm square) rearranged pixels(to keep reasonable size files). A difficulty arose at that step due to the rather small dynamical range of the Reticon which saturates beyond d=2. The science plates have a rather high sky background, and hence, should be scanned with the light sources of the microdensitometer rated at a high voltage. On the other hand, the spot sensitometer plates exhibit a clear background which require, for a correct determination of the fog level, a scanning with the light source rated at a lower voltage. The maximum density range measurable with the MAMA when scanning the

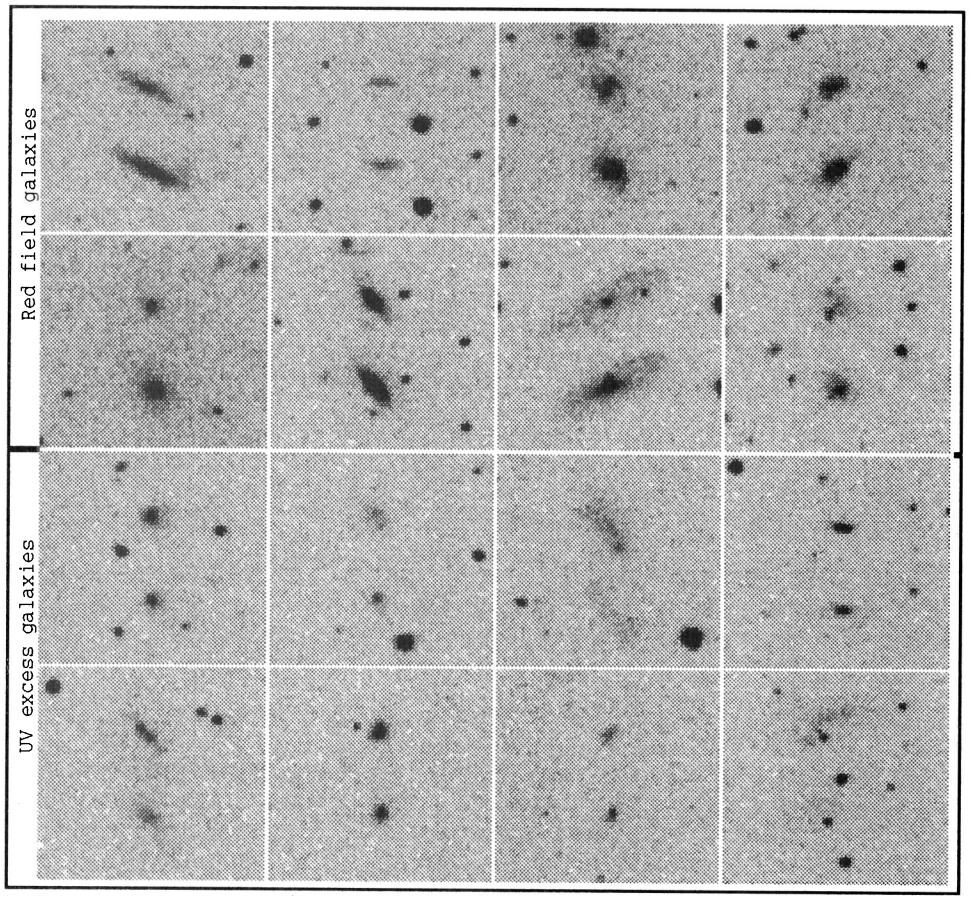

Fig. 2. Bicolor images of galaxies (U exposure: upper image. R exposure: lower image) *top rows*: red field galaxies *bottom rows*: ultraviolet excess galaxies not detected as emission line objects on the objective-prism plates

science plates is still larger than the useful range necessary to avoid saturation either on the star spectra, the galaxy spectra or the direct images of most objects (see also the discussion in Sect. 5.4). Each spot sensitometer plate was scanned twice, with the light source rated at the two different voltages. The measurements of some 6 to 8 spots whose densities fall in both cases in the normal dynamic range of the Reticon enables to derive a constant offset between the densities measured with both voltages of the light source. This offset is subtracted from the densities measured with the weak voltage and the density table is then homogenized.

The photographic density (d)-incident energy intensity (E) characteristic curve d = f (log E) is fitted through the measurements using Toraldo di Francia formalism as developed by Llebaria et al. (1981).

An interesting result is that for IIIaF emulsion, the characteristic curves in U and R passbands are very similar. This allows to superimpose them by a simple translation in log E (within the measurement errors). Figure 3 shows the characteristic curve relative to the IIIaF emulsion used for the two fields.

For IIIaJ emulsion, the slopes differ only slightly, and the same procedure has been used taking into account the effective range of photographic density on the spectra of the science plates. This leads us to a maximum uncertainty of 30% in the internal flux calibration affecting the brightest spectra

4. Redshift measurements

Although there exists a long tradition of stellar radial velocity determination from objective prism photographic plates, direct measurement of galaxy redshifts from objective prism Schmidt plates have been seldom undertaken. Previous attempts have been made for instance by Wasilewski (1983), Moss et al. (1988). Recently a systematic program has been launched at the University of Muenster (Seitter et al. 1989; Tucholke & Schuecker 1992) using lower dispersion plates. Quasar redshifts have been produced with automated reduction methods by Clowes et al. (1980) and Hewett et al. (1985)

4.1. Co-addition of prism plates block scans

To improve the signal to noise ratio for each emission-line candidate, the twin objective prism block scans are coadded with a procedure which deserves a detailed description. First, the sky background is evaluated on each intensity calibrated block scan by means of simple statistics on a series of selected sky areas. The two independant averaged sky values are compared.

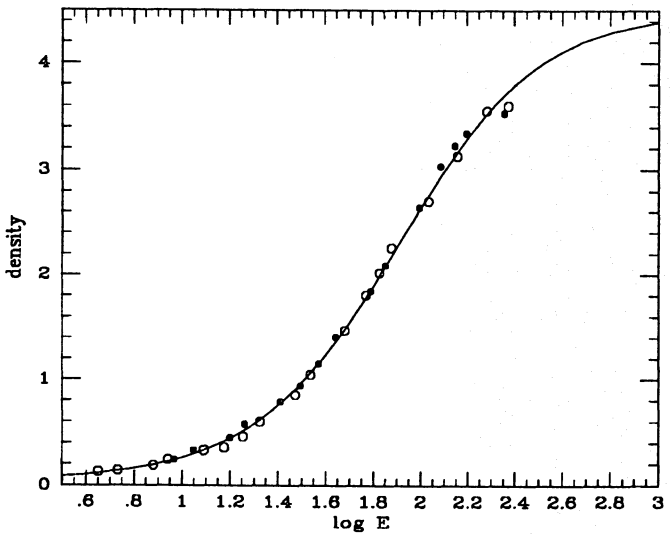

Fig. 3. Density-intensity calibration curve for Kodak IIIaf emulsion used for the photometric reduction of the bicolor direct images. *dots*: spot sensitometer exposure through the R 630 filter *circles*: spot sensitometer exposure through the UG 11 filter The R and U experimental calibrations have been superimposed by a translation of the U curve along the log E axis. The continuous line is the adopted common best fit valid for both passbands

Their ratio, close to 1, is used to equalize the sky background of the two files. The Y and X reference points necessary for the coaddition are derived as follows (X axis is defined as the direction of the prism dispersion, Y axis is defined as the direction perpendicular to the prism dispersion):

An identical rectangular subimage, approximately centered on the same region, is extracted from both block scans. Each subimage is compressed along the direction of the prism dispersion by averaging its columns so that each spectrum of a field star is reduced to a spike-like trace in the resulting compressed (1 dimension) image. The centers of these traces are derived by means of a gaussian fitting routine. The difference, in abscissa, between the couple of traces originating from spectra of a same star on the two plates gives an offset value. Averaging this offset on all the couples of avaible star traces, we get the correction to apply to the Y coordinate of one of the two block scans with a standard deviation of $\frac{1}{10}$ of a pixel. Further, one of the block scans is repeatedly subtracted from the other, incrementing the X start coordinate until the mean, the sum of the highest intensity pixels (higher than the mean value) and the standard deviation of the distribution of the pixel values, in the difference image, are minimized. Upon convergence one gets the X offset between the two block scans with an accuracy of $\frac{1}{6}$ of a pixel.

In what follows, the term block scan will refer to the result of the coaddition.

4.2. *Wavelength calibration*

Local distortions on prism plates may be introduced by various causes (plates curved during exposures and measured flat, prism inhomogeneities, residual aberrations of the optical combination, possible imperfect alignment of the plateholder, etc..). These problems have been studied in astrometric work (see e.g. Smith 1975; Fresneau 1978) and in stellar radial velocity work (see e.g. Stock 1992 and references therein). Further, the ESO Schmidt corrector is not achromatic, and this induces variable image quality along the spectrum. Therefore, a metrological use of these plates, as required to derive accurate redshifts from the spectra, implies a thorough wavelength calibration procedure. Performing such a calibration over the entire area of a Schmidt plate leads to tedious numerical modeling and is better suited to fully automated reduction methods as derived for instance by Moss et al. (1988) or Hewett et al. (1985). In the following we have adopted a "local calibration" approach deriving an independent calibration over each plate area covered by a block-scan. The relation which expresses the separation ΔX, along the direction of dispersion between two spectral lines, in a spectrum obtained with a prism of small angle A is:

$$\Delta X = X_2 - X_1 = f \cdot A \cdot |n_{\lambda_2} - n_{\lambda_1}| \quad (1)$$

where $\lambda_1 = \lambda_{1t} \cdot (1+z)$ and $\lambda_2 = \lambda_{2t} \cdot (1+z)$, λ_{it} is the theoretical wavelength, z the redshift, f the Schmidt telescope focal length, A the prism angle, X_i the position on the plate for the wavelength λ_i and n_{λ_i} the prism refractive index for the wavelength λ_i. The value of n_{λ_i} depends only on the prism material, and may be computed with a high precision as a λ dependent function. In Schott technical notices, a polynomial approximation is given, yielding n_{λ_i} with an accuracy of 10^{-5} for the UBK7 prism material.

Hence, the basic step in the calibration process is the evaluation of the product of the focal distance by the prism angle of the Schmidt telescope ($f \cdot A$). An error of 1 arc minute on the prism angle value induces a global error on velocity of about 580 km s^{-1}. The only available calibrators are the spectra of the field stars. In each block scan, G-K type stars (the most common) with well defined absorption lines are selected. In order to improve the signal to noise ratio, we built a composite spectrum from 5 to 8 of these stars in each block scan, coadding the extracted spectra after alignment on the very deep CaII H line core.

Then, assuming the average radial velocity of the Galactic stars, used as calibrators, to be zero, it is possible to find out the local value of the $f \cdot A$ product, by solving Eq.1 for each couple of lines of the composite spectrum. A 1.5 sigma rejection cycle is applied to the series of $f \cdot A$ values in order to derive the adopted local average $f \cdot A$ product. The exact value of each of the parameters A and f is not useful, but we derived the following estimate for the prism angle, averaged over 80 independent block scans:

$$< A >= 4^\circ\, 02'\, 35'' \pm 09''$$

(assuming a focal length f = 3055.7 mm as given in the ESO User's Manual). This value is in a perfect agreement with the value given by the technical commissioning report of the Schmidt telescope (Schuster, private communication).

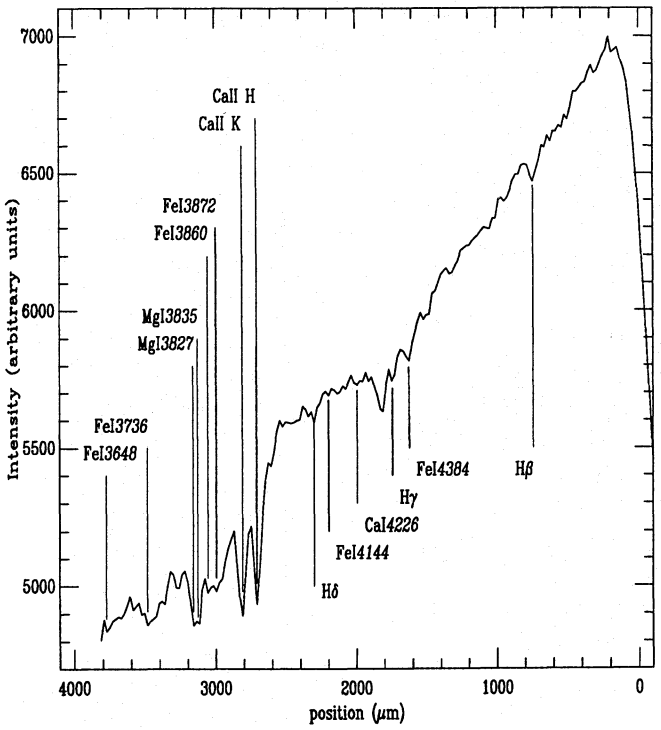

Fig. 4. Stellar composite spectrum built using 8 G-K type stars; lines used for the wavelength calibration are indicated. The G band has a somewhat variable contrast on the plates depending on the spectral type and also on the stellar brightness. This induce a slightly variable "effective" wavelength for the feature, so we decided not to use it in the calibration

We found no evidence of systematic pattern in the observed deviations between the local $f \cdot A$ values and the average value computed for one field. The observing procedure is such that each plate of the pair is taken on each side of the meridian passage of the field. The subsequent addition of the original block scans before wavelength calibration possibly blurs out part of the systematic pattern, if any exists and if it is due to mechanical flexures in the instrument.

4.3. Redshift derivation

Once obtained the local value of the $f \cdot A$ product, the redshifts are derived using two different procedures:

- Thanks to the non linear dispersion of the objective prism, the distance between two lines on a same spectrum depends on their respective wavelengths, and hence on the radial velocity of the object. Using Eq. 1, with the distances between the emission lines [OIII]5007Å, [OIII]4959Å, H_β and [OII]3728Å, when present, it is possible to derive up to 6 redshift values, but, due to the much lower dispersion at the green end of the spectrum, a redshift obtained from the difference in position between H_β and [OIII], or between the two lines of [OIII], will have a poor accuracy. Therefore we limit the redshift determination to the use of 3 values using [OII]3728Å and each one of the other lines. When [OII]3728Å is not present, it is better to use the second procedure described below.

Using ponderation weights (function of the signal to noise ratio of the emission line) we deduce an averaged redshift z_I.

All emission line positions are measured using Gaussian fits as performed by MIDAS routines.

- The second procedure uses both the objective prism and the bicolor plates. The size of the block scans is sufficiently small (10 arc minutes that is $\frac{1}{30}$ of the Schmidt field) so that a linear transformation model between prism and direct plates remains valid. From field star positions on the bicolor plate and CaII H line core position in their respective spectrum on the corresponding prism plate, we determine an average separation Δ_{Ca} along the dispersion direction. Using the position X_G of the galaxy image on the bicolor plate and Δ_{Ca} we can predict the coordinate of the CaII H line core of the galaxy spectrum for a recession velocity equal to zero. From Δ_ζ, distance between CaII H line and one of the emission lines of the galaxy at null velocity, we can compute the position at null velocity X_o, of any given wavelength:

$$X_o(\lambda) = X_G + \Delta_{Ca} + \Delta_\zeta(\lambda) \qquad (2)$$

With Eq.(1), in an iterative routine, we can get up to 4 values of the galaxy redshift if the 4 emission lines [OIII]5007Å, [OIII]4959Å, $H\beta$ and [OII]3728Å, are all present. As above, a weighted average gives the final value z_{II}. This second procedure could seem less precise than the first one, because it involves a coordinate transfer between plates taken with different optical configurations. But a comparison of the results shows excellent consistency with the first method involving only the prism plates. This procedure is useful for objects with only one spectral line detected. It can be applied for instance on galaxies showing the [OII]3728Å emission line, up to large values of redshifts.

In what follows redshifts are systematically expressed as heliocentric recession velocities because the presently detected objects span only a redshift range $z < 0.06$

The formal regression line gives:

$$V_{II} = 0.995\,(\pm 0.012)\,V_I + 36\,(\pm 503) \qquad (\text{in km s}^{-1})$$

Our final velocity values, V_{ours}, are weighted averages of velocities derived from both methods.

4.4. Comparison with published values

The velocities V_{ours} derived from the Schmidt plates have been compared with those published in the literature V_{lit} (de Vaucouleurs et al. 1990 (RC3), Dressler 1991).

This comparison is illustrated in Table 1 and Fig. 6

Unfortunately there are almost no redshift calibrators beyond $Z = 0.017$ in the sky areas corresponding to our two pilot fields. The Seyfert 1 galaxy M13.24 (Maza et al. 1991) rediscovered independantly by us, which exhibits H_β and H_γ broad lines at a recessional heliocentric velocity of 19020 km s^{-1} seems to confirm that both procedures are free from serious systematic errors. In Fig. 6, the formal regression line gives:

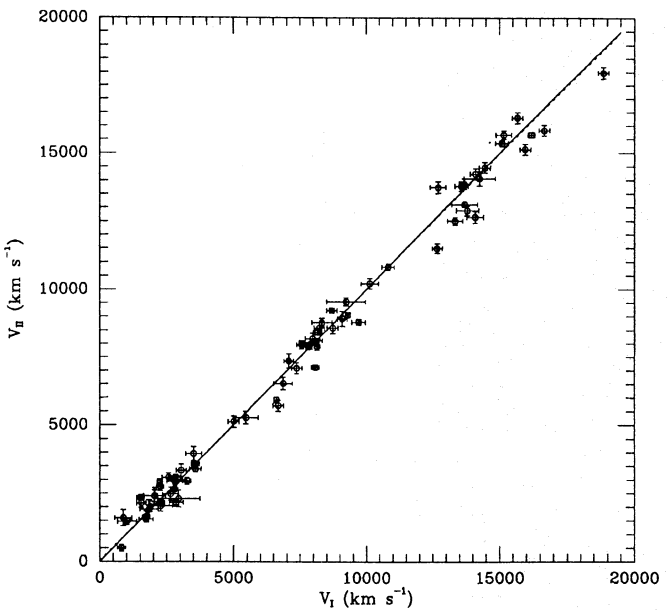

Fig. 5. Plot of experimental velocities V_{II} derived using second method versus experimental velocities V_I derived using the first method. Redshift values z_I and z_{II} have been converted into heliocentric recession velocities V_I and V_{II}

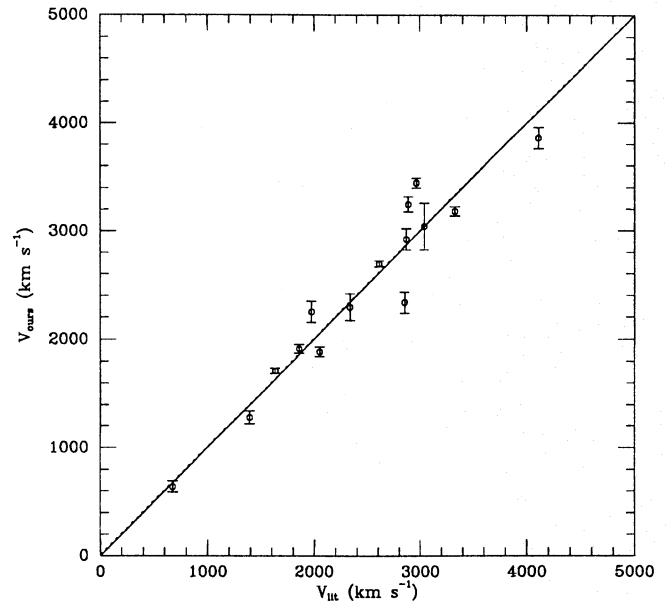

Fig. 6. Comparison between velocities derived from our study (V_{ours}) and those published in catalogs (V_{lit})

$$V_{ours} = 0.998\,(\pm 0.014)\,V_{lit} + 15\,(\pm 238) \qquad \text{(in km s}^{-1}\text{)}$$

implying that:

- the zero-point error is negligible on the objective-prism velocities.
- the accuracy of the two procedures are comparable.

Using the mean of the redshift values derived by both procedures, and comparing to the literature values on the sample of calibrators, we derive a final estimate of the accuracy of the redshifts:

$$\Delta v = 160 km\ s^{-1}$$

It should be underlined that this estimate of the accuracy is only valid up to cz = 5000 km s^{-1}. We can only check the precision with external calibrations as recession velocities measured independantly, either from HI 21 *cm* line, or from optical slit spectrography. More data are needed on a larger redshift range in order to be sure that our redshifts are really free from any systematic error.

5. Photometry

A set of MIDAS macroroutines has been developed to reduce the bicolor images of the galaxies.

5.1. Quick photometry

A kappa-sigma statistics is performed on a series of 3 to 6 rectangular windows of blank sky in the immediate vicinity of the object, each window containing a minimum of 200 pixels. The resulting average flux per pixel is taken as the local sky background value. An instrumental magnitude is derived by integrating the intensity of the objects pixels above a threshold defined as 1.5 times standard deviation, above the local sky background, and correcting the result from the contribution of the sky. This is done on the ultraviolet and red images of the galaxy. An estimate of the average surface brightness in the image is obtained by dividing the integrated flux corrected from the background contribution, by the number of pixels taken into account.

5.2. Surface photometry

A more elaborate photometry, performed by isophotal integration of the flux in the ultraviolet and red images of the galaxy, gives the following parameters:

- asymptotic magnitudes U_∞ and R_∞ obtained by extrapolation at large radius of the magnitude curve of growth by integrating in isophotes of fainter and fainter levels.
- effective radius. For each isophote, the equivalent radius is computed as:

$$r^* = \sqrt{\frac{A}{\pi}} \qquad (A \text{ being the isophote area})$$

The effective radius r_e^*, is defined as the equivalent radius containing half of the total light. In magnitudes:

$$U_e = U_\infty + 0.75$$

$$R_e = R_\infty + 0.75$$

The equivalent radius at $\frac{1}{4}$ and $\frac{3}{4}$ of the total light are also computed.

Table 1. identification of emission line galaxies, whose velocities have been previously measured. V_{lit} are the velocities from the literature V_{ours} are the average ones measured in our study **ΔV**: difference between our velocities and published ones **Error**: estimated error on each velocity [(1)]**MCG**: Morphological Catalog of Galaxies [(2)]**PGC**: Principal Galaxy Catalog (Paturel et al. 1990) [(3)]**M**: Calalan Tololo survey (Maza et al. 1989)

Object	Previous identification		V_{lit} (km s^{-1})	V_{ours} (km s^{-1})	ΔV (km s^{-1})	Error (km s^{-1})
1304-234	NGC4968	ESO508-G-E	2988 ±30	3044	+56	430
1305-226	MCG04-31-35[1]	ESO508-G-11	2608 ±30	2697	+87	52
1306-240	PGC45565[2]		4109	3861	−248	196
1306-241	MCG04-31-0037	ESO508-G-15	2872 ±30	2926	+54	196
1307-215	PGC45721	ESO576-G-3	2943 ±30	3249	+306	140
1307-240	MCG04-31-0040	ESO508-G-19	2967 ±30	3445	+478	92
1308-236	MCG04-31-0041	ESO508-G-24	2856 ±30	2337	−417	140
1309-250		M13.24[3]	19038 ±45	19020	−18	372
1312-237	MCG-04-31-0043	NGC5042	1388 ±30	1279	−109	120
1313-263		ESO508-G-33	3330	3181	−149	80
1314-276		ESO444-G-2	1631	1712	+64	46
1316-208	MCG-03-34-0046	NGC5068	671 ±30	638	−33	100
1317-258	PGC46551	ESO508-G-51	2135 ±30	1886	−249	88
1321-194	MCG03-34-69	ESO576-G-50	1983 ±30	2251	+269	200
1321-274	PGC46808		2340	2293	−47	228
1324-277	MCG05-32-0020	ESO444-G-3	1859	1914	+55	78
					$< \|\Delta V\| >$	$< Error >$
					165	**160**

- surface brightnesses: I_u and I_r being the intensity levels of a given isophote, I_{sky} being the local sky background, the surface brightness μ_u and μ_r are defined as:

$$\mu_u = -2.5\, log \frac{(I_u - I_{sky})}{1.825}$$

$$\mu_r = -2.5\, log \frac{(I_r - I_{sky})}{1.825}$$

in mag·arcsec^{-2}. (The factor 1.8225 is the pixel size in arcsec^2). $m_{u,e}$ and $m_{r,e}$ are the mean surface brightness inside the effective isophote (directly computed by dividing half of the total flux corresponding to magnitudes U_∞ or R_∞ by the area of the effective isophote, πr_e^{*2}). $\mu_{u,e}$ and $\mu_{r,e}$ are the "effective" surface brightness, i.e $\mu_u(r^* = r_e^*)$ and $\mu_r(r = r_e^*)$. Theyare interpolated on a plot of $\mu(r^*)$ versus r^*. Tables containing the curve of growth for U and R magnitudes and μ_u and μ_r surface brightnesses are kept for each object to fit with $r^{\frac{1}{4}}$ or exponential laws if required. These procedures remain partly interactive. In order to reduce the amount of computer time necessary to process hundreds of images, the isophotal integration is limited to 6 to 12 isophote steps depending on the size and brightness gradient of the object.

5.3. Color calibration

The quick as well as the surface photometry produce results in instrumental units. Up to now, we have not undertaken any CCD imaging follow-up on these fields. However we tried to assess a color and magnitude calibration linking our instrumental system to a standard one.

The color calibration is derived using the field stars in a statistical approach based on the Basel RGU photometry. We know that we may encounter some problems by performing photometry of extended sources on Schmidt plates if the calibration of magnitudes is done with stellar standard sequences, because of the particular shape of stellar images given by the Schmidt optics. These problems are essentially due to the use of a quite small number of bright calibrators. The situation can improve with a larger number of faint stellars calibrators whose density of central pixels remains moderate on the emulsion. Further, we decided to limit the use of the stars to the color scale calibration.

The Basel photometric system consists on 3 photographic passbands R, G, U and has been widely used for the study of the Galactic stellar population, at various Galactic latitudes. We assumed as working hypothesis that:

- our instrumental color U-R could be linked to the Basel color through a linear relation, because our plate-filter combination, although different from the Basel standard combinations, gives quite comparable resulting passbands, as explained above.

- the Galactic stellar population has approximately the same U-R color distribution at symmetric Galactic latitudes. The stellar population in our fields located at an average $b = -40°$ should thus exhibit a color distribution consistent with that exhibited in Basel field SA107 at b = +41° (Becker & Fenkart 1976; Becker & Steppe 1977).

We used a variant of the quick photometry procedure (in which the detection threshold is suppressed) on a large number of block scans from the bicolor plate thus measuring a large number of field stars. Care was taken to exclude any star whose central pixel(s) would have an intensity corresponding to a photographic density larger than 2.0, in order to keep the measurements on the well-defined and linear part of the characteristic curve of the IIIaF emulsion (see Fig. 3). Figure 7 shows the histogram of instrumental U-R colors obtained for 1612 stars. An histogram of the Basel U-R colors observed in the field SA107 was built from the data of Becker & Fenkart (1976) and is also displayed on fig 7. Both histograms exhibit similar overall shapes implying that the working hypothesis outlined above were acceptable: the Kendall's statistical test gives a τ value of 0.98 (the maximum value is 1 for identical shapes). However we note that our instrumental histogram has a slightly wider peak, followed by a deficit in very red stars, with respect to the Basel color distribution. The deficit in red stars is readily explainable by a selection effect in our data. We use bi-color plates and limit the photometry to moderately exposed stars images. Very red faint stars have nearly undetectable ultraviolet images and hence are automatically excluded from the stellar photometry. In turn, part of this deficit can, through the normalization process, be reflected into a broader maximum in the range of color which corresponds to the most easily measurable star image couples. The area corresponding to each block scan from a bicolor plate is carefully inspected on the ESO-SRC J sky survey films, in order to select the galaxies for the quick photometry. Therefore, confusion between faint background galaxies (which would be largely undetectable) and stars remain marginal and is unlikely to lead to substantial errors. By selecting brighter magnitude limits in the star sample, the agreement improves only marginally. Therefore we suspect, either a subtle effect of the difference between our passbands and those of Basel, or a real difference in the stellar populations between our fields and SA107, or a combination of both. The shift of the instrumental color histogram along the color axis, to match the Basel color histogram (until the residuals are minimized), gives the zero point of our color scale:

$$(U-R)_{Basel} = (U-R)_{instr} + 2.29\,(\pm 0.05)$$

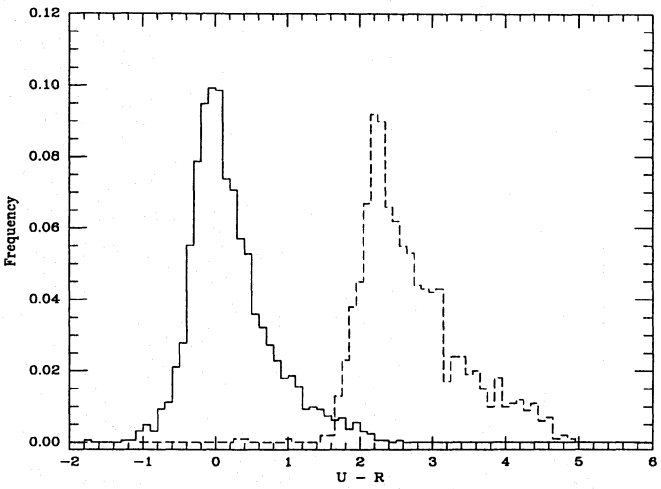

Fig. 7. Histogram of instrumental U-R color (solid line) based on 1612 stars and the one in Basel color (dashed line) based on 1000 stars from the field SA107 published by Becker & Fenkart (1976)

The formal error estimate is based on the width of the minimal residual zone along the color axis and is only valid for stellar images.

Because of the possible problems when treating extended sources, we shall consider that the accuracy of this color zero point, when applied to galaxies cannot be better than 0.10 mag. Plate-to-plate variations may also degrade this accuracy. CCD photometry on a sample of our galaxies would of course provide a better calibration.

The definition of our zero point is tied to the Basel system which is based on U - R = 0.00 for a B0 V star (Becker 1946; Steinlin 1968). Steinlin (1968) also provides revised transformation equations of Johnson U B V colors into Basel colors through the relation:

$$(U-R)_{Basel} = 1.04\,(U-B) + 1.22\,(B-V) + 1.56$$

An A0 V star ($(U-B) = 0$ and $(B-V) = 0$, in the Johnson system), will thus have $(U\text{-}R)_{Basel} = 1.56$. This transformation relation enables to derive an approximate spectral type matching to the Basel U-R color scale (fig 10).

5.4. Calibration of the magnitudes

The surface photometry procedure has been used on ultraviolet-excess and other field galaxies which are present in the ESO-LV photometric catalogue (Lauberts & Valentijn 1989). The asymptotic magnitudes in our instrumental R band were directly compared to the ESO-LV total (asymptotic) R magnitudes. We limit the comparison to small angular diameter galaxies whose twin images remain sufficiently unblended on the bicolor plates. However, the offset of the telescope between the two exposures being only 30", a residual merging of the outer isophotes in the two images is difficult to avoid and has been empirically corrected when necessary. Hence the number of available standards in a field was reduced to a small sample of objects. Figure 7 shows the provisional relation between ESO-LV values and

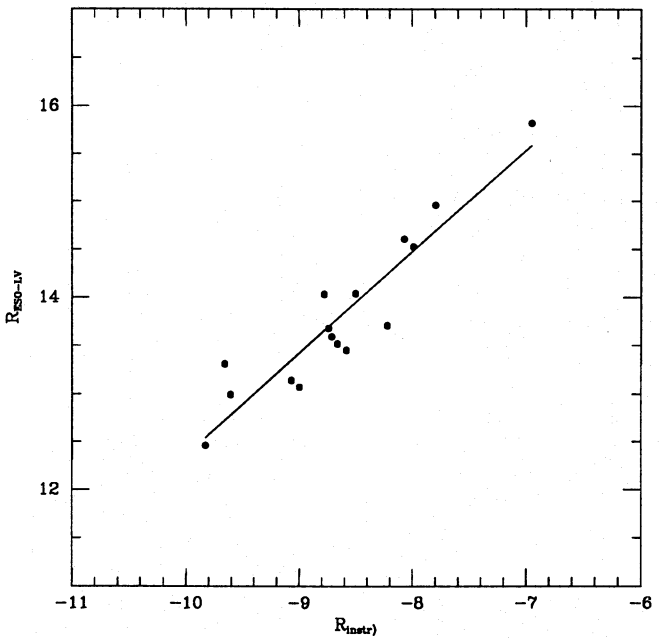

Fig. 8. R magnitude calibration using ESO-LV magnitudes. The line is the best fit with slope equal to 1

ours based on 16 galaxies located in one of the fields. A least-squares fit to a linear relation gives:

$$R_{ESO} = 1.06\,(\pm 0.11)\,R_{inst} + 22.93\,(\pm 0.96)$$

It should be underlined that the R band used in the ESO-LV photometric catalog is tied to the Cousins R band and hence is different from the Basel R band which we use for color study purpose only. Note that we did not try to compare our quick magnitude estimates to ESO-LV magnitudes because they are more or less isophotal values and not asymptotic values. The slope does not appear significantly different from the expected value of unity. The large value of the error affecting the zero point is probably partly due to the problems in performing the photometry of extended images which are not completely isolated. Another known cause of error is the uncertainty in the extrapolation process leading to the derivation of the asymptotic magnitude. If we force the slope to be equal to one, the derived zero point is equal to 22.44 (±0.10). Note however that:

- there is only one calibrator for magnitudes larger than R_{ESO} = 15.0, while the bulk of our ultraviolet excess galaxy population is fainter than this value,

- this result being limited to one field, there may exist plate-to-plate variations leading to external errors not yet investigated.

This magnitude calibration will be better defined as measurements of a larger number of galaxies in several fields become available.

Let us assume that the above calibration holds up to the faint end of the distribution of apparent instrumental magnitudes and that the practical limit of our photometry (defined by the acceptable level of signal-to-noise ratio for an extended object) corresponds to an instrumental magnitude of -4.0. We conclude that the limiting measurable magnitude of the red galaxy images on the bicolor plates is about R = 18.5 (in Cousins system). One may question the validity of this extrapolation. The local sky background has a photographic density level around 0.4 - 0.5 (most of the variations being due to local plate sensitivity variations: see Lauberts & Valentijn (1989), for a discussion), while the brightest pixels in the galaxy images have d =1.7 to 1.8. The faintest measurable galaxies have most of their pixels at a few flux units (10^{logE}) above the sky, that is, their photographic density implies an intensity conversion using the low flux, non-linear part of the characteristic curve of the emulsion (see Fig. 3). However, this section of the characteristic curve is well constrained by the sensitometer calibration measurements and density measurement errors due to the narrow dynamic range of the Reticon of the MAMA do not occur in this range, but in the large density (and large log E) part of the curve. This problem of non-linear conversion occurs also on the outermost isophotes of the brighter galaxies. It is quite difficult to assess the accuracy of our instrumental R magnitudes. The local sky background is derived with an accuracy of some 3% while the average probable error in extrapolating the magnitude growth curve may be evaluated as 0.15 magnitude. However, this does not take into account the error due to improper correction of the parasitic contribution of faint isophotes of the ultraviolet image of a galaxy into its red image. Further, our plate calibration is much less elaborated than that performed by Lauberts & Valentijn (1989) who claim an accuracy of 0.09 on their asymptotic magnitudes. We may assume that our internal accuracy is 0.30 magnitude. Considering all the measurable galaxies, for faint objects the main difficulty is a correct extrapolation of the curve of growth, while for bright objects the main cause of error is the blending of the U and R outer isophotes. CCD follow-up of a subsample of the uv-excess galaxies is mandatory to improve this situation by deriving a set of empirical corrections depending e.g. on surface brightness and apparent isophotal diameter.

Work is also in progress to derive B magnitudes for all our ultraviolet excess and emission line candidates by performing the same surface photometry on glass copies of the ESO-SRC J Sky Survey.

6. First results

To illustrate the description of the methods used both in redshift measurement and photometry, we give some preliminary results on the two fields reduced insofar. The redshift sample is complete for both fields, but up to now we have photometric data only on one bicolor plate. A more detailed astrophysical analysis will appear elsewhere. In particular, the discussion of selection effects and completeness criteria of our survey is postponed until we have the complete set of photometric data at our disposal. Additional data retrieval on the prism plates (continuum magnitude estimates and measurements of equivalent widths of the emission lines) is also in progress.

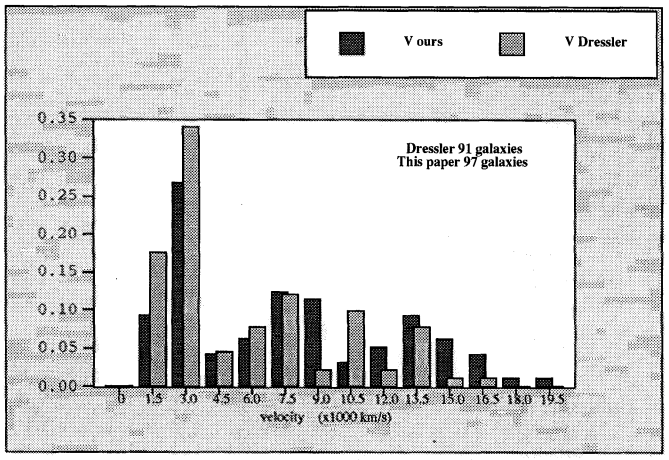

Fig. 9. Normalized histogram of the measured redshifts: comparison is done with the Dressler sample (1991) in the same sky area bounded to $13^h\,02 < \alpha < 13^h\,23$ and $-22°\,00' < \delta < -27°\,40'$. Bin size is 1500 km s $^{-1}$

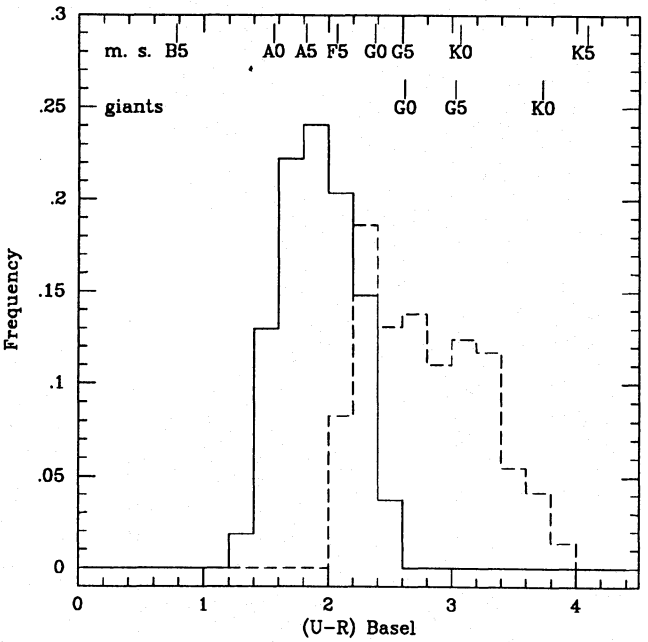

Fig. 10. Color disrtribution and mean stellar-type calibration (solid line: "UV excess galaxies", dashed line: "red galaxies" the histograms are respectively normalized on 145 red galaxies and 54 ultraviolet excess galaxies

6.1. Redshifts

Figure 8 is an histogram of the redshifts measured on the objective prism plates. We derive radial velocities for a total of 97 emission line galaxies (some of them are normal spirals exhibiting bright HII regions in their arms). The comparison is made with all the galaxies published by Dressler (1991), in the same sky area. Note that there is almost no overlap between Dressler's sample and ours. The shape of both histograms is similar till 10,000 km s^{-1}. Beyond this value we still have a number of high velocity objects, implying a deeper sounding of space by means of the active galaxy population.

6.2. Photometry

Figure 10 shows the color distribution (obtained with the quick photometry procedure) of the objects selected with the microscope as ultraviolet excess galaxies in relation to normal field galaxies observed in the same block scans. The mean spectral type scale displayed on the figure, derived from the Johnson colors transformed to Basel colors shows that:

- the dominant population in ordinary red field galaxies is composed of G K giants (as expected)

- ultraviolet excess galaxies, on the other hand, are dominated by a main sequence population. This population, in the integrated light, is not hotter than A0. Hence, when emission lines are present in the spectrum, implying the presence of O B stars, this massive, hot population contributes only moderately to the integrated light in the visible. The near ultraviolet is also not very sensitive to the O B population, because of the large number of A - F stars accompanying the massive O B stars in the initial mass function of the starburst. The histograms overlap significantly for $2.00 < (U - R) < 2.60$. This is due to the definition of what we call an ultraviolet excess object. Of course there is no discontinuity in the color distribution of a galaxian population. The eye selection procedure is such that we classify as ultraviolet excess objects some galaxies in which only parts of the image are bluer than the remaining pixels (e.g blue nuclei objects or, on the contrary, blue extended disks surrounding red bulges) as well as objects whose entire image exhibit ultraviolet excess. The measurement performed by the quick photometry corresponds more or less to the evaluation of the average color of the object.

A more elaborated, quantitative separation of the ultraviolet excess objects will be done in the final catalog, on the basis of the colors measured by means of the surface photometry procedure.

7. Conclusions

A search for active star-forming galaxies has been conducted with the ESO 1 meter Schmidt telescope, combining the detection of emission-line objects with the large 4 degrees objective-prism and the detection of ultraviolet-excess galaxies by means of the U and R two-color direct photography.

We have developed a complete reduction scheme for the Schmidt plates which allows to process photographic spectra and two-color images of a large number of extragalactic objects. It has been elaborated to produce a maximum astrophysical output before any subsequent follow-up, providing accurate redshifts, magnitudes, colors and morphological parameters.

Figure 11 summarizes the data extraction process in a flowchart.

We measured redshifts for 97 emission lines galaxies with an accuracy of 160 km s^{-1}. Some 500 ultraviolet excess galaxies have been found in 50 square degrees. The photometry of these objects is in progress, yielding asymptotic magnitudes with a

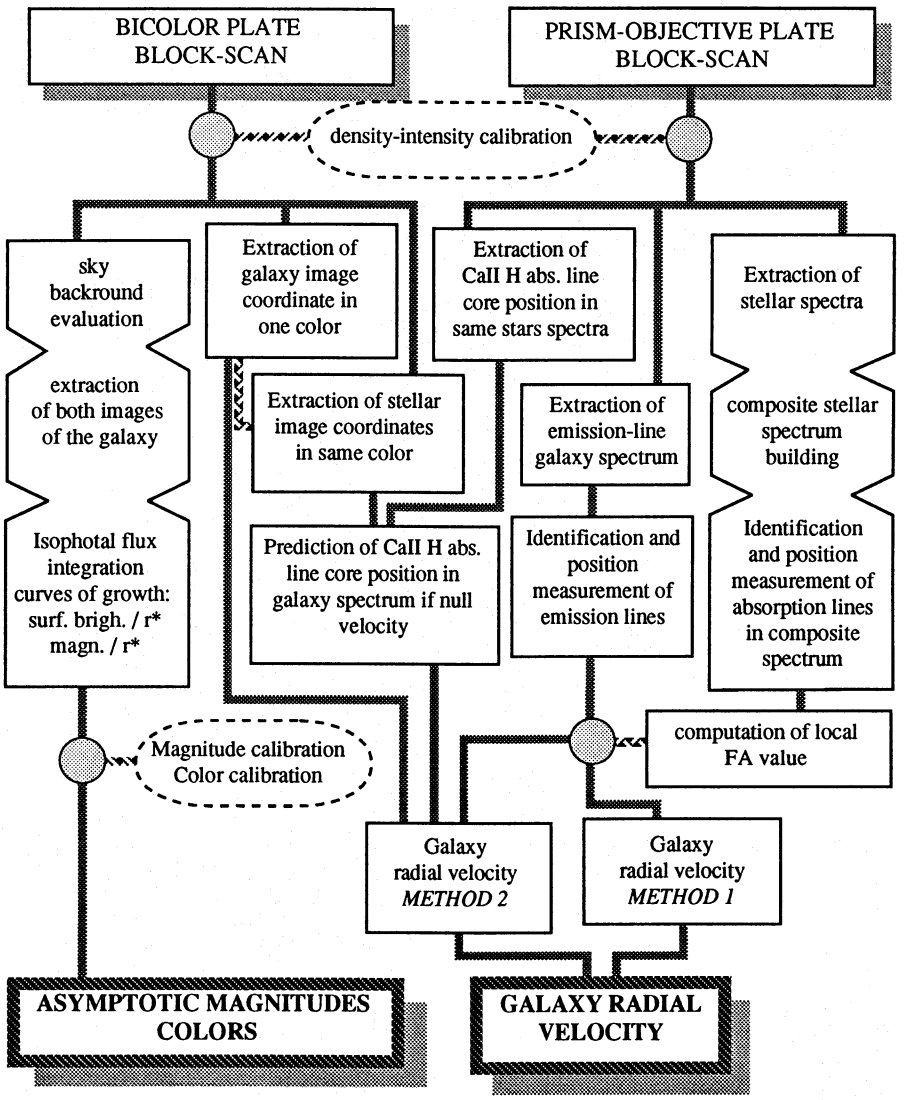

Fig. 11. Flow-chart of the data processing

probable accuracy of about 0.30 mag, colors and various other parameters. The U-R color of these galaxies is tied to the Basel system with a zero-point accuracy of about 0.10 mag. These first results extracted from the two pilot fields make us very confident in our ability to retrieve useful statistical astrophysical results on the properties of the population of faint star-forming low redshift galaxies.

The data processing scheme, initially designed for the present study, is not specific to Schmidt photographic plates. It could be used, with only minor modifications, for the reduction of slitless field spectroscopy and wide field imaging performed on telescopes equipped with two dimensional digital detectors.

Statistical studies on starburst galaxies need as large, deep and complete samples of galaxies as possible. To these ends, Schmidt surveys still remain competitive with larger instruments. Associating deep bicolor survey and emission line objects search, we expect to find a large sample of different active galaxy types, from low luminosity spirals or circumnuclear HII regions to Blue Compact Dwarf Galaxies, with a fair sampling of the starburst age distribution. The recent advent of fast microdensitometers enables a very thorough data retrieval. Hence Schmidt surveys still seem far from being out of date, especially for extragalactic statistical investigations. The foreseeable progressive use of CCD large arrays at the foci of large Schmidt telescopes in a near future will certainly open new fascinating possibilities.

Acknowledgements. The observations with the Schmidt Telescope have been conducted by the ESO staff at La Silla. We warmly thank H-E Schuster, O. and G. Pizarro for efforts leading to the obtention of plate material of outstanding quality. We thank the invaluable help of J. Guibert and the MAMA staff during the crucial phase of plate digitization. Photometry of large numbers of objects has been performed at Institut d'Astrophysique de Paris (I.A.P) by C. Oberto whose skill and perseverance is gratefully acknowledged. This work benefited from numerous stimulating discussions with D. Kunth and J. Guibert and from the support of A. Omont, Director of Institut d'Astrophysique de Paris.

References

Augarde R., Chalabaev A., Comte G., Kunth D., Maehara H. 1993, A&AS (submitted)

Becker W. 1946, Veroff. Univ. Sternwarte Göttingen, 79

Becker W., Fenkart R. 1976, Photometric catalog for stars in selected areas and other fields in the RGU system, Publ. of. Astr. Institute of the University of Basel.

Becker W., Steppe H. 1977, A&AS 28, 377

Berger J., Cordoni J.P., Fringant A.M., Guibert J., Moreau O., Reboul, H., Vanderriest C. 1991, A&AS 87, 389

Clowes R.G., Emerson D., Smith M.G., Wallace P.J.,Cannon R.D., Savage A., Boksenberg A. 1980, MNRAS 193, 415

Comte G., Augarde R., Chalabaev A., Kunth D., Maehara H. 1993, A&A (submitted)

Da Costa, L.N., Pellegrini, P.S., Davis, M., Meiskin, A., Sargent W.L.W., Tonry, J.L. 1991, ApJS 75, 935

Dressler A. 1991, ApJS 75, 241

Fresneau A. 1978, AJ 83, 406

Guibert J., Charvin, P., Stoclet, P. 1984, in Astronomy with Schmidt Type Telescopes, M. Capaccioli editor, Reidel, p.165

Guibert J., Moreau O. 1991, The ESo Messenger 64 p.69.

Hewett P.C., Irwin M.J., Bunclark P., Bridgeland M.T., Kibblewhite E.J., He X.T., Smith M.G. 1985, MNRAS 213, 971

Høg E., von der Heide J. et al. 1976, Abhandlungen Hamburger Sternwarte IX (PERTH70)

Huchra J.P. 1977, ApJS 35, 171

Lauberts A. & Valentijn E.A. 1989, Surface Photometry Catalogue of the ESO Uppsala Galaxies, ESO

Llebaria A., Figon P. 1981, Astronomical Photography 1981, J.L. Heudier, M.E. Sim eds, CNRS, p. 25

Markarian B.E., Stepanyan D.A. 1983, Afz 19, 639

Mass-Hesse J.M., Kunth D. 1991, A&AS 88, 399

Maza J., Ruiz M.T. 1989, ApJS 69, 353

Maza J., Ruiz M.T., Gonzalez L.E, Wiscrnjewsky M. 1989, ApJS 69, 349

Moss C., Whittle M., Irwin,M.J. 1988 MNRAS 232, 381

Olofsson K. 1989, A&AS 80, 317

Pesch P., Sanduleak N. 1983 ApJS 51, 171

Paturel G., Fouqué P., Bottinelli L., Gouguenheim L. 1989, Catalogue of Principal Galaxies, Observatoire de Lyon

Salzer J.J. 1990, ApJ 347, 152

Seitter W.C., Ott H.A., Duemmler R., Schuecker P., Horstman H.,1989, in Morphological Cosmology, P. Flin and H.W. Duerbeck eds, Springer, p. 3.

Smith M.G. 1975, ApJ 202, 591

Soubiran C. 1992, A&A 259, 394

Steinlin U.W. 1968, Z. fr Astrophys. 69, 276

Stock J. 1992, RMAA 24, 45

Terlevich R., Melnick J., Masegosa J., Moles M., Copetti M.V.F. 1991, A&AS 91, 285

Tucholke H.J., Schuecker P. 1992, PASP 104, 704.

Vaucouleurs G. de, Vaucouleurs A. de, Corwin H.G.Jr., Buta R.J., Paturel, G., Fouqué P. 1991, 3rd Reference catalog of Bright Galaxies (RC3), Springer-Verlag

Wasilewski A.J. 1983, ApJ 272, 68

White S. D. M. 1988, in The Epoch of Galaxy Formation, Frenk et al. eds., Kluwer, p.15

This article was processed by the author using Springer-Verlag TEX A&A macro package 1992.